Accepted Manuscript

Multifunctional applications of self - Assembled 3D CeO_2: Cr^{3+} hierarchical structures synthesized via ultrasound assisted sonochemical route

B.S. Rohini, H. Nagabhushana, G.P. Darshan, R.B. Basavaraj, S.C. Sharma, P. Amudha, M. Rahul, B. Daruka Prasad

PII: S0925-8388(17)32418-0

DOI: 10.1016/j.jallcom.2017.07.054

Reference: JALCOM 42470

To appear in: *Journal of Alloys and Compounds*

Received Date: 31 March 2017

Revised Date: 25 June 2017

Accepted Date: 6 July 2017

Please cite this article as: B.S. Rohini, H. Nagabhushana, G.P. Darshan, R.B. Basavaraj, S.C. Sharma, P. Amudha, M. Rahul, B. Daruka Prasad, Multifunctional applications of self - Assembled 3D CeO_2: Cr^{3+} hierarchical structures synthesized via ultrasound assisted sonochemical route, *Journal of Alloys and Compounds* (2017), doi: 10.1016/j.jallcom.2017.07.054.

This is a PDF file of an unedited manuscript that has been accepted for publication. As a service to our customers we are providing this early version of the manuscript. The manuscript will undergo copyediting, typesetting, and review of the resulting proof before it is published in its final form. Please note that during the production process errors may be discovered which could affect the content, and all legal disclaimers that apply to the journal pertain.

Graphical Abstract

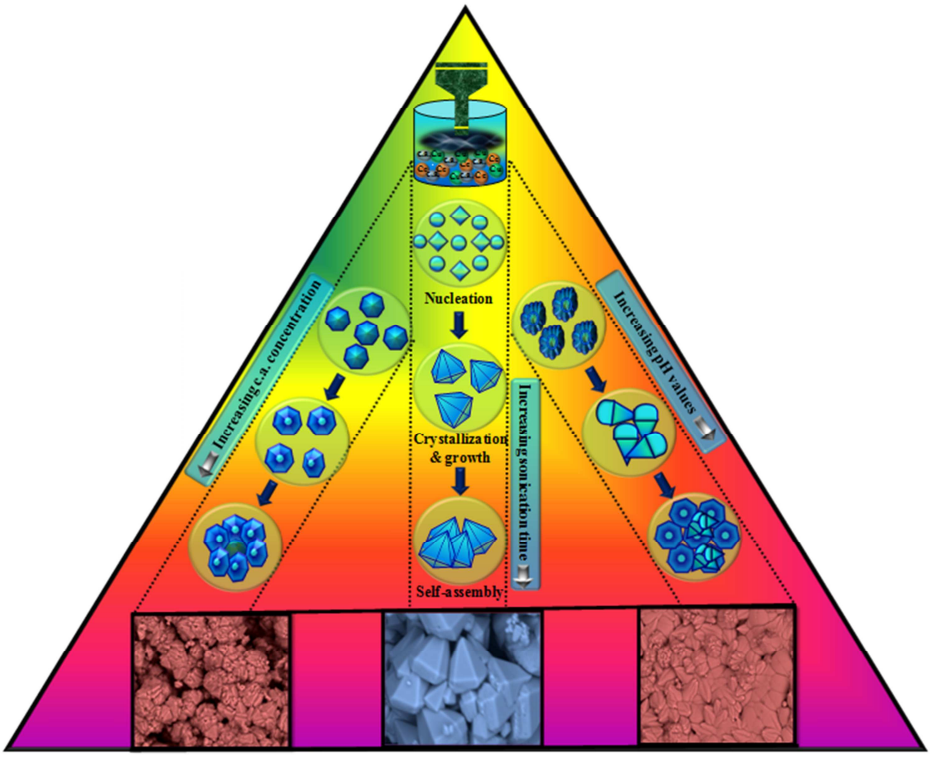

ACCEPTED MANUSCRIPT

ACCEPTED MANUSCRIPT

Multifunctional applications of self - assembled 3D CeO_2: Cr^{3+} hierarchical structures synthesized via ultrasound assisted sonochemical route

B.S. Rohini[1], H. Nagabhushana[1,*], G.P. Darshan[2], R.B. Basavaraj[1], S.C. Sharma[3,4], P.Amudha[5], M. Rahul[6], B. Daruka Prasad[7]

[1]Prof. C.N.R. Rao Centre for Advanced Materials Research, Tumkur University, Tumkur 572 103, India
[2]Department of Physics, Acharya Institute of Graduate Studies, Bangalore 560 107, India
[3]Department of Mechanical Engineering Jain University, Advisor, Jain group of Institutions, Bangalore 560069, India
[4]Advisor, Avinashilingam Institute for Home Science and Higher Education for Women University, Coimbatore 641043, India
[5]Department of Computer Science and Engineering, Avinashilingam Institute for Home Science and Higher Education for Women University, Coimbatore 641043, India
[6]Department of Mechanical Engineering, Mazda B & C Block, Gopalan global axis, White field, Bangalore 560066, India
[7]Department of Physics, BMS Institute of Technology and Management, VTU-affiliated, Bangalore 560 064, India

Abstract

In the present work, CeO_2:Cr^{3+} (1-11 mol %) nanophosphors (NPs) were prepared via eco-friendly ultrasound assisted sonochemical route using *Cicer arietinum (C.A.)* seeds extract as surfactant. The PXRD results confirm the pure cubic structure with average crystallite size was found to be ~ 6 - 10 nm. The optical energy band gap (E_g) were estimated and found to be ~ 2.95-3.45eV. Three-dimensional (3D) hierarchical nanostructures are considered as new probe due to their high surface areas and exhibits distinctive properties which furnish excellent performance in luminescent applications. The effect of various experimental parameters on growth mechanism of 3D morphology of the product was extensively studied. Raman studies confirm the incorporation of Cr^{3+} ions into the CeO_2 matrix, possible electronic states during excitation, oxygen vacancies and defect sites available. PL studies have shown an intense sharp peak at ~ 689 nm along with vibrancies side bands at ~ 706 and 734 nm. A ~ 689 nm peak was well known R – line and was assigned to the $^2E_g \rightarrow {}^4A_{2g}$ transition of Cr^{3+} ions. The crystal field splitting and Racah parameters were calculated to know the inter-electrons repulsion in host lattice. The CIE chromaticity co-ordinates were located in pure red region. Further, CCT values were in the range 5342 – 7781 K. The optimal CeO_2:Cr^{3+} (9 mol %) NP was successfully explored as a fluorescent probe for visualization of latent fingerprints (LFPs) on both porous and non-porous surfaces. Aforementioned studies indicate that the prepared sample were quite useful for multifunctional applications namely display devices and forensic applications.

Key words: Hierarchical structures, Latent fingerprint, Photoluminescence, display devices.

* Corresponding author: +91-9945954010, E-mail: bhushanvlc@gmail.com (Dr. H. Nagabhushana).

1. Introduction

Recently, nanocrystalline Cerium dioxide (CeO_2) material creates numerous interests because of its fluorite-type structure, notable redox nature and major oxygen storage and release capacity (OSC) through superficial change between Ce^{4+} state and Ce^{3+} oxidation state [1-3]. The CeO_2 material have wide spread of applications including catalysts, solar cells, ultraviolet (UV) blocking filters, gas sensors and etc. [4-7]. In nanocrystalline CeO_2, oxygen vacancies lead to oxygen conduction. Mainly, the control of morphology and crystallite size on the property of ceria leads to considerable significance due to grain boundaries reactions and significant depletion of carriers in anisotropic nanosystems can effectively changes the redox/transport nature. Non - stoichiometric nature of CeO_2 was more prominent in nanocrystalline form due to its enhanced surface to volume ratio results decrease of crystallite size leads to reduction of formation energy of oxygen vacancies [8]. As a result, the variation in the electronic density due to residual electrons reside in a 4f electron energy state of cerium ions surrounded by newly existed vacancy site and reduce Ce^{4+} ions to the Ce^{3+} state. These added electrons occupy the cerium ions sites that are first or second nearest neighbors of vacancy sites [9, 10] whereas it is also possible for some electrons to be localized on the oxygen vacancies.

Normally, chromium ions were often chosen as impurities since they exhibit +1, +3, +4 and +6 oxidation states, where Cr^{3+} ions were considered to be more stable oxidation state which can be extensively employed as an inexpensive activator for the enhancement of luminescence properties [11]. Significant amount of work has been documented in the literature for the fabrication of oxide phosphors by wet chemical routes [12, 13]. However, a few reports are available for the synthesis of metal oxide hierarchical structures by facile ultrasound assisted sonochemical method. In sonochemical method three important events may occurs namely,

acoustic cavity formation, resulting in bubbles formation at the surface and impulsive collapse of these bubbles in the solution. These exciting factors are responsible in the formation of different architectures of the nanomaterials. Size distribution, shape and size of the nanopowders can be tuned by varying different experimental conditions in the sonochemical method namely, surfactant concentration, sonication time, pH value of the precursor solution etc. [14]. In the recent years, bio-surfactants (leaf/root/latex/seed extracts) were extensively used for the synthesis of nanomaterials as they are eco - friendly, cost-effectiveness, quick and large quantities production of NP with systematically altering the precursors [15]. Further, the method offers a numerous advantages other others namely eco-friendly, cost effective, less energy consumption and etc. Further, added advantage of use of bio-surfactants for the synthesis of nanomaterials they serve not only as a reducing agent but also acts as capping agents [16, 17].

The *C.A.* seed contains high protein and dietary fiber and hence it was used for treating number of diseases as abortifacient, hair tonic, useful in cold pains etc. The seeds were useful in vitiated condition of pitta, bronchitis, inflammations and skin diseases. Further, the seeds contain various phytochemicals namely proteins (20 – 23 %), carbohydrates (41.1 – 47.42 %), fiber (6 % crude fiber), minerals (phosphorus, calcium, magnesium, iron and zinc), β – carotene and etc. [18]. Isoflavones are the main bio-active components of sprouted chickpea seeds. They have gained considerable importance due to the diverse and broad biological activities, including anti oxidative, oestrogenic, insecticidal, piscicidal, antifungal, antimicrobial and contraceptive properties. Presence of these isoflavones in the seed extract particularly Calycosin helps in obtaining the various hierarchical structures [19]. Table.1 shows the major bio-active compounds in the *C.A.* seed extract.

Usually, the lean of human fingers consists of well characterized complicated skin pattern due elevated papillary ridges and miserable furrows in the skin [20]. These ridge patterns were differing not only from person to person but also from finger to finger. When the finger made to contact with surfaces, the constituents of fingers such as sweat, oily substances and etc derived from eccrine and sebum glands were transferred and deposited onto the surface, leads to formation of a fingerprint (FP) [21]. Due to unique, immutable and complex property, since FPs are considered as major tool in forensic science, making of identity document (ID), access control for some special regions/buildings and border entry at the immigration. Moreover, FPs investigations in a crime spot are regarded as solid evidence for identification of individuals in forensic department [22].

During crime spot investigation, usually three different types of FPs were observed including impression, patent and LFPs. Amongst, LFPs are the most regular at crime scenes and are invisible to human eye [23]. Therefore, to make them visualize several techniques including optical, physical, and chemical processes have been employed. However, many researchers have made several attempts to visualize LFPs which will assist for advanced forensic investigations and to boost the success rate. Among them, powder dusting, cyanoacrylate fuming, ninhydrin method, 1, 8-Diazafluoren-9-one method, silver nitrate method, and small particle reagent method, are the most extensively used methods due to simple experimental procedure, efficiency and sensitivity. Even though, these convectional visualize methods have several drawbacks namely low contrast, less selectivity and high toxicity [24]. To overcome from these problems, fluorescent labeling powders are considered to be most efficient and significant agents for visualize LFPs on both porous and non-porous surfaces owing to their distinctive optical and chemical properties [25]. These labeling powders exhibits several benefits namely smaller

crystallite size, exceptional photo- chemical stability, enhanced luminescence property, morphological variations and low toxic nature [26].

In our present work, we report for the first time a facile and efficient route to fabricate $CeO_2:Cr^{3+}$ (1 - 11 mol %) NPs with 3D hierarchical structure by ultrasound assisted sonochemical method using *C.A.* seed extract as a surfactant. Variation in oxygen vacancies concentration and active oxygen species on the crystal was due to changes in the dopant Cr^{3+} ion concentration are extensively studied. The application of prepared optimized $CeO_2:Cr^{3+}$ (9 mol %) NP for visualization of LFPs on various porous and non – porous surfaces was established.

2. Experimental and characterization

The seeds of *C.A.* were procured in Tumkur local market, Karnataka. The procured seeds were thoroughly washed using double distilled water and keep for dry at room temperature (RT). By using sterilized blender the seeds were grounded to form a fine powder and stored in an air tight container. The *C.A.* powder (10 g) was mixed with 100 ml double distilled water and mixed thoroughly using magnetic stirrer until aqueous solution turn from black to light yellowish brown color. Then, the resultant extract was cooled, filtered and used for further experiments.

The materials used in the present study are AR grade cerium nitrate ($Ce(NO_3)_2 \cdot 6H_2O$; 99.99%), and chromium nitrate ($Cr(NO_3)_3 \cdot 9H_2O$; 99.99%) procured from Sigma Aldrich Ltd. The stoichiometric amount of cerium nitrate and chromium nitrate were well dissolved in a double distilled water using magnetic stirrer to get homogeneous mixture. Further, different concentration of *C.A.* seed extract (5- 30 % W/V) was mixed with precursor solution slowly and pH level (1, 5, 7, and 9) of the solution was maintained by adding NaOH under constant stirring. Then, the resultant solution was irradiated with ultrasound (frequency ~ 20 kHz, power ~ 300 W)

at constant temperature of 80 °C. The same procedure was repeated for various sonication irradiation times (1- 6 h). The final precipitate solution was filtered and washed in distilled water. The obtained powder was dried at 80 °C and further calcined at ~ 700 ^{o}C for 3 h.

All the LFPs were collected from different donors. The hands of the donor thoroughly washed with soap and cleaned with water, propanol, and ethanol. Then, washed hands were dried in air, gently rubbed on forehead and deposited on various forensic related surfaces. The prepared CeO_2:Cr^{3+} (9 mol %) NP was carefully stained on LFPs and excess powder was removed by smooth brushing method. The visualization of FP images was recorded under UV 254 nm light by using 50 mm f/2.8G ED lens Nikon D3100/AF-S digital camera.

The powder x-ray diffraction (PXRD) studies were performed by using Shimadzu X-ray diffractometer (PXRD-7000) using CuK_{α} radiation (λ=1.541 Å) with a nickel filter to know the crystallinity and phase of the prepared samples. Morphology of the samples studied by scanning electron microscope (SEM, Hitachi TM -3000 model) and transmission electron microscopy (TEM, TECNAI F-30 model). The Lambda-35 (PerkinElmer) spectrophotometer was used to record diffuse reflectance (DR) spectra of the samples. Fluorolog-3 Jobin Yvon Spectroflourimeter with 450 W Xenon lamp as an excitation source was used to Photoluminescence (PL) studies. The Fourier transform infrared spectra were recorded in Bruker alpha made FTIR instrument. The Jobin YVON Horiba LABRAM-HR-Visible micro Raman system is used for Raman studies with He-Ne laser (~ 632.8 nm) as the source.

3. Results and Discussions

The PXRD profile of pure and CeO_2:Cr^{3+} (1- 11 mol %) NPs were shown in Fig.1 (a). All the diffracted peaks were well indexed to cubic phase of ceria with space group Fm-3m (225) and

were good agreement with standard JCPDS card (No. 34-0394) [27]. The sharp and intense diffracted peaks of prepared samples imply high crystallinity. The peaks intensities corresponding to crystal planes (111), (200), (220), (311) and (222) for all the samples does not exhibit much difference, indicating that there is no preferred orientation or orientation crystal growth. The highest intensity peak (111) was shifted towards lower angle side as concentration of dopant increases due to substitution of dopant Cr^{3+} ions into the host leads to expansion of crystal lattice. From Fig.1 (a), it was evident that substitution of dopant (Cr^{3+}) ions into host lattice did not manipulate the crystal structure but changes its lattice parameters because of ionic radii mismatch [28, 29]. The average crystallite size (D) of CeO_2: Cr^{3+} (1-11 mol %) NPs were estimated using Scherrer's relation [30]:

$$D = 0.9\lambda / \beta \cos\theta \quad \text{---------- (1)}$$

where, λ ; wavelength of the X-rays, β ; the full- width at half maximum (FWHM) and θ ; the angle of diffraction. The average crystallite size of CeO_2: Cr^{3+} (1-11 mol %) NPs were estimated and listed in Table 2. The FWHM of a peak at ~ 28.2° was found to enlarged with increase of Cr^{3+} ions concentration and was mainly attributed to micro-strain present in the samples. To estimate the value of 'D' as well as micro – strain present in the prepared samples, Williamson – Hall (W - H) fitting method was used [31]:

$$\beta \cos\theta = \varepsilon \left(4 \sin\theta\right) + \frac{\lambda}{D} \quad \text{---------- (2)}$$

where β*;* FWHM in radians, ε ; the strain, *D*; the crystallite size and θ; Bragg's diffraction angle. The value of 'D' and micro – strain present in the product was estimated and tabulated in Table 2. The W-H plots were shown in Fig. 1 (b). The reduced value of crystallite size with increase in

Cr^{3+} content was due to oxygen vacancies because of compact radius of Cr^{3+} ions (0.52 Å) compared to Ce^{4+} (1.034 Å). Further, CeO_2: Cr^{3+} (3, 5, 9 mol %) NPs exhibit negative slope which indicate that the presence of compressive strain in the samples [32, 33]. The acceptable percentage difference (D_r) between dopant ions and host was estimated to know the effective substitution of Cr^{3+} ions at Ce^{4+} symmetry site by using following relation [34]:

$$D_r = \frac{R_m - R_d}{R_m} \text{ ---------- (3)}$$

where R_m; radii of host material (R_{Ce}^{4+} = 1.034 Å) and R_d; and radii of dopant ion (R_{Cr}^{3+} = 0.52 Å). The calculated value of 'D_r' was found to be ~ 19 %. This establishes that dopant Cr^{3+} ions were effectively substituted at Ce^{4+} symmetry site. But, the larger ionic radius difference between Cr^{3+} ion and Ce^{4+} cause a contraction of the host lattice leads to larger proportion in the composition [35].

The cubic fluorite structure of the prepared samples was confirmed through structural Rietveld refinement by using *Fullprof suit Program* as shown in Fig.1 (c). In the face-centered cubic fluorite structure of CeO_2, eight oxygen elements occupy tetrahedral positions and surrounded on a cerium. Each oxygen elements has four ligancy of cerium cations. As a result, added oxygen vacancies were created after dopant Cr^{3+} ions were substituted in the host lattice. When the concentration of Cr^{3+} ions increase without altering experimental parameters, significant variation in the lattice parameter was observed (Table 3). The GOF (goodness of fit) was used ensure superiority of the refined data. The estimated GOF was found to be ~ 0.32, which confirms good fitting of experimental and theoretical plots. The packing diagram was drawn from the *Diamond* software and was shown in inset Fig.1 (c).

Fig.2 (a) shows diffuse reflectance (DR) spectra of the CeO_2: Cr^{3+} (3-11 mol %) NPs. The absorption bands recorded at ~ 360 and 566 nm were attributed to $^4A_{2g}(F) \rightarrow {}^4T_{1g}(F)$ and $^4A_{2g}(F) \rightarrow {}^4T_{2g}(F)$ spin-allowed d-d transitions of Cr^{3+} ions respectively [36]. By making use of Kubelka-Munk (K-M) theory, direct energy gap (E_g) of prepared CeO_2: Cr^{3+} (3-11 mol %) NPs were estimated. The relation between K - M function $F(R_\infty)$ and photon energy ($h\nu$) was reported elsewhere [37]. By plotting a graph of $F(R)^2$ versus $h\nu$ and extrapolating the linear fitted regions to $F(R)^2=0$, the E_g values were estimated (Fig.2(b)) and presented in Table 2. A small change in estimated E_g values was mainly due to oxygen vacancies present in the samples.

Fig.2(c) depicts the Raman spectra of CeO_2: Cr^{3+} (1 - 11 mol %) NPs measured in the range 350–800 cm^{-1}. A strong peak at ~ 464 cm^{-1} was assigned to F_{2g} vibration of the cubic fluorite-type structure and it can be considered as the symmetric stretching mode of oxygen atoms around cerium ions. A weak peak at ~ 478 cm^{-1} was due to non - degenerate longitudinal optical mode caused by a local Ce-O (R_{Ce-O}) bond symmetry stretch. The formation of intrinsic oxygen vacancies due to escape of lattice oxygen from the cubic structure results to maintain electrically neutralize particles [38]. A very weak peak at ~ 470 cm^{-1} was observed and attributed to extrinsic oxygen vacancies cause by doping (R_{dopant}). To maintain electronic neutrality particles, dopant Cr^{3+} ions offers different valence states with Ce^{4+} and hence fraction of oxygen would escape from the host lattice leads to formation of extrinsic oxygen vacancies. The relative intensities of Raman peaks at ~ 464, 478 and 470 cm^{-1} can be estimated by using following relation [39]:

$$\frac{Oxygen\ vacancies}{F_{2g}} = \frac{\left(Area_{R_{Ce-O}} + Area_{R_{dopant}}\right)}{Area\,F_{2g}} \text{ ---------- (4)}$$

The calculated values were listed in Table 2. It was evident that, oxygen vacancies were increases as a concentration of Cr^{3+} increases upto 9 mol % was due to consequence of only

extrinsic oxygen vacancies and apart from the intrinsic oxygen vacancies. With further increase of Cr^{3+} concentration, oxygen vacancies decreased in order to maintain neutrality of the prepared product.

The FTIR spectra of CeO_2: Cr^{3+} (1-11 mol %) NPs recorded in the range 400–4000 cm^{-1} were depicted in Fig.2 (d). The broad band ~ 3390 cm^{-1} was assigned to O–H stretching mode [40]. A CO_2 band at ~ 1346 cm^{-1} may arise because of trapped CO_2 in air condition. The band at ~ 1650 cm^{-1} corresponds to the bending of H–O–H and partly overlapping the O–C–O stretching band. The band at ~ 390 cm^{-1} was due to the stretching mode of Ce–O [41]. The proteins and carbohydrates present in FTIR studies may offers constancy to the escalation of CeO_2 nanostructures by avoiding agglomeration. The alkaloids and flavonoids present in a seed extract having functional groups such as O–C–O, -C-O-C- and -C-O- may afford capping action and supports to growth of nanostructure [42]. In addition, the amino, carboxylic and phenolic functional groups of seed extract could also be liable for the construction of diverse shaped CeO_2 nanostructures.

SEM micrographs of CeO_2: Cr^{3+} (9 mol %) NP fabricated with different sonication time (1 – 6 h) with 30 % W/V concentration of *C.A.* seed extract and pH value =13 were shown in Fig.3. When ultrasound irradiation time was at 1 and 2 h, growth staged hexagonal - like structures were observed (Fig.3 (a & b)). As the irradiation time was extended to 3 and 4 h, hexagonal - like structures were undergo further growth, and start oriented in order direction was observed in Fig.3 (c & d). Further, when the ultrasonic irradiation time was still prolonged to 5 and 6 h, the orderly oriented self- assembled hexagonal - like structures were observed (Fig.3 (e & f)). Thus, it was confirmed that the ultrasound irradiation time for the synthesis hierarchical structures play a vital role.

Fig.4. shows the effect of various concentration of *C.A.* seed extract on morphology of CeO_2: Cr^{3+} (9 mol %) NP prepared with 6 h ultrasonic irradiation time and pH = 13. When the *C.A.* seed extract concentration is 5 and 10 % W/V, hexagonal pud like structures was observed (Fig. 4(a & b)). However, self- assembled ripen pud like structures were observed, when the concentration of *C.A.* seed extract was increased to 15 and 20 % W/V (Fig. 4 (c & d)). Further, increase of *C.A.* seed extract concentration to 25 and 30 % W/V, almost flower –like 3D hierarchical structures was observed (Fig.4 (e & f)). The effect of *C.A.* seed extract for the formation of 3D superstructures can be was explained by model called egg box model, where the polymeric network of the contents of the *C.A.* seed extract wrap into complex network of in which the CeO_2:Cr^{3+} ions gets trapped leaving behind the various hierarchical structures as depicted in Fig.5.

The effect pH value on morphology of the product by altering size and shape due to various factors including crystal- face attraction, electrostatic and dipolar fields associated with the aggregate, Vander Waals forces, intrinsic structures and external factors leads to hierarchical structures. When NaOH level of the precursor solution was maintained at 3, 5 and 7, hallow spherical - like structures were observed (Fig.6 (a, b & c)). As the pH of the solution was increased to 9 and 11, self – assembled cone - like hierarchical structures were observed (Fig.6 (d & e)). Further, pH was increased to 13, the well oriented cones form flower like 3D - superstructures were observed in Fig.6 (f). These results were evident that the pH value has played vital role in tuning the morphology of the product. The schematic representation for nucleation, growth and self-assembly of structures to form 3D - hierarchical structures with various experimental parameters was shown in Fig.7.

The TEM image of $CeO_2:Cr^{3+}$ (9 mol %) NP (Fig. 8 (a & b)) shows that the particles were nearly hexagonal in shape. HRTEM image of $CeO_2:Cr^{3+}$ (9 mol %) NP was shown in Fig. 8 (c). Well - defined short range arrangement of atomic planes with inter planar spacing (d) ~ 0.31 nm confirms the crystalline nature of the sample. The SAED pattern of the optimized NP confirms the crystalline nature and all circles were matched with the (hkl) planes of the PXRD graph (Fig. 8 (d)).

Fig.9 (a) shows the photoluminescence (PL) excitation spectrum of $CeO_2:Cr^{3+}$ (9 mol %) NP under λ_{emi} = 689 nm. The spectra exhibits of intensive peaks at ~ 372 and 471 nm were attributed to $^4A_2\,(^4F) \rightarrow {}^4T_1\,(^4P)$ and $^4A_2\,(^4F) \rightarrow {}^4T_2\,(^4F)$ spin-allowed transitions respectively [43]. The PL emission spectra of $CeO_2:Cr^{3+}$ (1-11 mol %) NPs excited at 471 nm in RT was depicts in Fig.9 (b). An intense emission peak at ~ 689 nm was recorded for all the samples attributed to spin-forbidden $^2E_g \rightarrow {}^4A_{2g}$ transition of Cr^{3+} ions. A weak peak ~ 704 nm and broader peak ~ 734 nm were also recorded and ascribed to Cr^{3+} - Cr^{3+} pair interactions [44]. Fig.10 (a) shows the schematic representation of Tanabe - Sugano energy level diagram to show energy levels splitting. The variation of PL intensity with various Cr^{3+} ions concentration was studied and presented in Fig.10 (b). It was evident that, the PL intensity increases up to 9 mol % Cr^{3+} ions concentration and thereafter, it declines due to concentration quenching phenomena [43]. To know more about concentration quenching phenomena, it was very significant to explore the interaction behavior, which usually takes place due to radiation re-absorption, exchange interactions and electric multipolar interaction. The critical distance (R_c) distance between Cr^{3+} ions was estimated by using following relation [45]:

$$R_c = 2\left(3V/4\pi NX_c\right)^{1/3} \text{ ---------- (5)}$$

where V; unit cell volume, X_c; Cr^{3+} ions concentration and N; number of crystallographic sites per unit cell. By substituting the values of V; 161.70 $Å^3$, X_c; ~ 0.09 and N; 4, the estimated value of R_c was found to be ~ 18.50 Å which was much greater than 5 Å results multipole–multipole interaction [46].

According to ligand field theory, environmental effects of Cr^{3+} ions were expressed by the magnitude of the crystal field splitting parameter (D_q) and Racah inter-electronic repulsion parameter (B) [47]. The D_q value was obtained from the energy of the transition $^4A_{2g} \rightarrow {}^4T_{1g}$ by using following relation:

$$D_q = E\left({}^4A_{2g} \rightarrow {}^4T_{1g}\right) \Big/ 10 \text{ ---------- (6)}$$

The value of B was estimated from the observed energy bands using the relation [48]:

$$B = (2\gamma_1^2 + \gamma_{21}^2 - 3\gamma_1\gamma_2)/(15\gamma_2 - 27\gamma_1) \text{ ---------- (7)}$$

where γ_1 and γ_2; the energies corresponding to $^4A_{2g} \rightarrow {}^4T_{1g}$ and $^4A_{2g} \rightarrow {}^2T_{1g}$ respectively. The value of B evaluated was found to be ~ 151 cm^{-1} which was much lower than the free ion value of Cr^{3+} ion (918 cm^{-1}). Normally, for weak, strong and intermediate crystal field sites the values of $D_q/B < 2.3$, > 2.3 and $= 2.3$ respectively. The obtained value of D_q/B in the present work was estimated to be ~ 15.76, which indicates that Cr^{3+} ions situated in strong crystal field. It also evident that, PL property was mainly due to a spin and parity forbidden transitions of Cr^{3+} ions [48].

To estimate the color emission of the synthesized samples, the Commission International de I'Eclairage (CIE) 1931 chromaticity co- ordinates were estimated and the CIE diagram of $CeO_2:Cr^{3+}$ (1-11 mol %) NPs were shown in Fig.10 (c). The corresponding co- ordinates were presented in Table 4. It was clearly observed from the figure that, chromaticity co-ordinates were

located in the pure red region. Correlated color temperature (CCT) was estimated by CIE co-ordinates (Fig. 10(d)) to estimate the applicability of the prepared NPs. The light emitted can be converted in terms of CCT by using the McCamy empirical formula [49]. If the lamp CCT value was less than 5000 K then it was considered as "warm" light sources and the lamps with CCT value greater than 5000 K was considered as "cool" in appearance [50]. The estimated CCT values were listed in Table 4. Color purities of the obtained sample were also estimated by using relation.

$$\text{Colour purity} = \frac{\sqrt{(x_s - x_i)^2 + (y_s - y_i)^2}}{\sqrt{(x_d - x_i)^2 + (y_d - y_i)^2}} \quad \text{---------- (8)}$$

where (x_s, y_s) and (x_d, y_d) ; the co-ordinates of the sample point and dominant wavelength and (x_i, y_i) ; the co-ordinates corresponds to the highest illumination points. The estimated color purity of the prepared samples was listed in Table 4. Further, quantum efficiency (QE) of the optimized $CeO_2:Cr^{3+}$ (9 mol %) NP was estimated by the method described by De Mello [51] and Palsson [52]:

$$QE = \frac{\text{Number of photons emitted}}{\text{Number of photons absorbed}} = \frac{E_c - E_a}{L_a - L_c} \text{- - - - - (9)}$$

where, E_C ; the integrated luminescence of the phosphor caused by direct excitation, E_a ; the integrated luminescence from the empty integrating sphere (blank, without sample), L_a; the integrated excitation profile from the empty integrating sphere, L_c; the integrated excitation profile when the sample is directly excited by the incident beam. In the present case, the estimated value of QE was found to be ~ 63.25 %, suggest the high QE of the prepared sample.

However, in our previous studies the QE was found to be 65 %, 61 % for MgO:Dy^{3+}, CeO_2:Eu^{3+} and $YAlO_3$:Ho^{3+} [53-55] respectively.

Fig. 11 shows LFPs visualized by optimized CeO_2:Cr^{3+} (9 mol %) NP on various non-porous surfaces including glass, plastic sheet, steel scale, aluminum foil and coin. Fig.11 (a) shows the LFP on glass visualized by optimized sample under visible light. It was clearly evident that, FP image with level 2 ridge patterns such as hook, bifurcation, lake, bridge, etc, were enhanced. Conversely, the same fluorescent FP images on glass, plastic sheet, steel scale, aluminum foil and coin under UV 254 nm light also evidently visualized with minutiae level 2 ridge patterns due to their smaller crystalline size and high fluorescence property (Fig. 11 (b-f)). Hence, our prepared optimized CeO_2:Cr^{3+} (9 mol %) NP was considered to be a new probe for visualization of LFPs on various surfaces.

Similarly, the visualization of LFPs on porous surfaces was practically challenged for developers due to absorption of the constituents of LFPs by these materials. To evaluate the versatility of the prepared sample, LFPs were visualized on different porous surfaces with dissimilar background colors (Fig.12). Interestingly, high contrast, sufficient quality clearer ridge patterns on all surfaces were evidently determined without any background interference. Aforementioned results evident that, the present optimized NP can be used as a cool pure red component in lighting, display devices and forensic applications.

4. Conclusion

The CeO_2:Cr^{3+} (1-11 mol %) NPs were synthesized by a facile ultrasound assisted sonochemical route using *C.A.* seed extract as surfactant. A single phase cubic fluorite structure was confirmed by PXRD studies. When the concentration of Cr^{3+} ions increases without altering any other experimental parameters, significant variations in the lattice parameters were observed. Raman studies confirm the existence of all the possible defect sites, oxygen vacancies and type of bonds. The peak at ~ 464 cm^{-1} was attributed to F_{2g} vibration of the cubic fluorite-type structure and it can be considered as the symmetric stretching mode of oxygen atoms around cerium ions. A weak peak at ~ 600 cm^{-1} was due to non-degenerate longitudinal optical mode caused by a local Ce-O (R_{Ce-O}) bond symmetry stretch. The PL emission intensity increases up to 9 mol % with increase Cr^{3+} ion concentrations and thereafter, it decreases due to concentration quenching. The LFPs were visualized by using optimized NP on various porous and non- porous surfaces with high contrast, sensitivity, without any background interference. Also, the prepared phosphors were quite functional for cool phosphor for WLED's and forensic applications.

Acknowledgement

The author Dr. H Nagabhushana thanks VGST, Govt. of Karnataka, India [VGST/KFIST-4/GRD-489] for the sanction of this Project.

References:

1. T. Taniguchi, Y. Sonoda, M. Echikawa, Y. Watanabe, K. Hatakeyama, S. Ida, M. Koinuma, Y. Matsumoto, ACS Appl. Mater. Interfaces 4 (2012) 1010–1015.
2. Shih-Yun Chen, Yi-Hsing Lu, Tzu-Wen Huang, Der-Chung Yan, Chung-Li Dong, J. Phys. Chem. C 114 (2010) 19576–19581.
3. F. Meng, C. Zhang, Q. Bo, Q. Zhang, Mat. Lett. 99 (2015) 5-7.
4. Faisal A. Al-Agel, Esam Al-Arfaj, Ahmed A. Al-Ghamdi, Barry D. Stein, Yaroslav Losovyj, Lyudmila M. Bronstein, F.S. Shokr, Waleed E. Mahmoud, Ceram. Int. 41 (2015) 1115-1119.
5. V.C Costa, F.S Lameiras, M.V.B Pinheiro, D.F Sousa, L.A.O Nunes, Y.R Shen, K.L Bray, J. Non-Cryst. Solids 273 (2000) 209-214.
6. P. Jasinski, T. Suzuki, H.U. Anderson, Sens. Actu. B 95 (2003) 73-77.
7. AvelinoCorma, Pedro Atienzar, Hermenegildo Garcia, Jean-Yves Chane-Ching, Nat. Mater. 3 (2004) 394-397.
8. Charles T. Campbell, Charles H. F. Peden, Science 309 (2005) 713-714.
9. D. Kavyashree, R. Ananda Kumari, H. Nagabhushana, S.C. Sharma, Y.S. Vidya, K.S. Anantharaju, B. Daruka Prasad, S.C. Prashantha, K. Lingaraju, H. Rajanaik, J. Lumin. 167 (2015) 91-100.
10. M. Ramesh, M. Anbuvannan, G. Viruthagiri, Spectrochim. Acta, Part A 136 (2015) 864-870.
11. P.C. Nagajyothi, T.N. Minh An, T.V.M. Sreekanth, Jae-il Lee, Dong Joo Lee, K.D. Lee, Mat. Lett. 108 (2013) 160-163.
12. D. Kishore, A.M. Kayastha, Food Chem. 134 (2012) 1650-1657.
13. J. K. Chavan, S. S. Kadam, D. K. Salunkhe, Larry R. Beuchat, C R C Critical Reviews In Food Science And Nutrition, 25 (1987) 107-158.
14. M. Venkataravanappa, H. Nagabhushana, B. Daruka Prasad, G.P. Darshan, R.B. Basavaraj, G.R. Vijayakumar, Ultrason. Sonochem. 34 (2017) 803-820.
15. A. Arumugam, C. Karthikeyan, A.S. Haja Hameed, K. Gopinath, S. Gowri, V. Karthika, Mater. Sci. Eng. C 49 (2015) 408-415.
16. J. Malleshappa, H. Nagabhushana, D. Kavyashree, S.C. Prashantha, C. Shivakumara, Spectrochim. Acta, Part A 145 (2015) 63-75.
17. X. Wu, Q. Liang, D. Weng, J. Fan, R. Ran, Catal. Today 126 (2007) 430-435.
18. F.A. Al-Agel, E. Al-Arfaj, A.A. Al-Ghamdi, Y. Losovyj, W.E. Mahmoud, J. Magn. Magn. Mater. 360 (2014) 73-79.
19. S. Zhao, L. Zhang, P. Gao, Z. Shao, Food Chem. 114 (2009) 869-873.
20. G.P. Darshan, H.B. Premkumar, H. Nagabhushana, S.C. Sharma, B. Daruka Prasad, S.C. Prashantha, R.B. Basavaraj, J. Alloys Compd. 686 (2016) 577-587.
21. G.P. Darshan, H.B. Premkumar, H. Nagabhushana, S.C. Sharma, S.C. Prashantha, B. Daruka Prasad, J. Colloid Interface Sci. 464 (2016) 206-218.
22. G.P. Darshan, H.B. Premkumar, H. Nagabhushana, S.C. Sharma, S.C. Prashantha, H.P. Nagaswarupa, B. Daruka Prasad, Dyes Pigm. 131 (2016) 268-281.
23. H. Nagabhushana, R.B. Basavaraj, B. Daruka Prasad, S.C. Sharma, H.B. Premkumar, Udayabhanu, G.R. Vijayakumar, J. Alloys Compd. 669 (2016) 232-239.
24. R.B Basavaraj, H. Nagabhushana, G.P. Darshan, B. Daruka Prasad, S.C. Sharma, K.N. Venkatachalaiah, J. Ind. Eng. Chem. 51 (2017) 90-105.
25. M. Dhanalakshmi, H. Nagabhushana, G.P. Darshan, R.B. Basavaraj, B. Daruka Prasad, J. Sci.: Adv. Mater. Devices 2 (2017) 22-33.

26. K.N. Venkatachalaiah, H. Nagabhushana, G.P. Darshan, R.B. Basavaraj, B. Daruka Prasad, Sens. Actu. B 251 (2017) 310–325.
27. S.K. Alla, K.K. Devarakonda, E.V.P. Komarala, R.K. Mandal, N.K. Prasad, Mater. Des. 114 (2017) 584-590.
28. M. Nakayama, M. Martin, Phys. Chem. Chem. Phys. 11 (2009) 3241-3249.
29. P. Singh, M.S. Hegde, J. Gopalakrishnan, Chem. Mater. 20 (2008) 7268–7273.
30. K.N. Venkatachalaiah, H. Nagabhushana, G.P. Darshan, R.B. Basavaraj, B. Daruka Prasad, S.C. Sharma, Spectrochim. Acta Part A: Mole. Biomole. Spect. 184 (2017) 89–100.
31. H.J. Amith Yadav, B. Eraiah, H. Nagabhushana, G.P. Darshan, B. Daruka Prasad, S.C. Sharma, H.B. Premkumar, K.S. Anantharaju, G.R. Vijayakumar, ACS Sustainable Chem. Eng. *5* (3) (2017) 2061–2074.
32. J. Malleshappa, H. Nagabhushana, S.C. Sharma, D.V. Sunitha, N. Dhananjaya, C. Shivakumara, B.M. Nagabhushana, J. Alloys Compd. 590 (2014) 131-139.
33. Prashant K. Sharma, Ranu K. Dutta, R. J. Choudhary, Avinash C. Pandey, CrystEngComm. 15 (2013) 4438-4447.
34. G.P. Darshan, H.B. Premkumar, H. Nagabhushana, S.C. Sharma, B. Daruka Prasad, S.C. Prashantha, Dyes Pigm. 134 (2016) 227-233.
35. H. Li, G. Wang, F. Zhang, Y.Cai, Y. Wang, I. Djerdj, RSC Adv. 2 (2012) 12413-12423.
36. L.R Shah, B. Ali, H. Zhu, W.G. Wang, Y.Q. Song, H.W. Zhang, S.I. Shah, J.Q. Xiao, J. Phys.: Condens. Matter, 21 (2009) 1-9.
37. C. Suresh, H. Nagabhushana, G.P. Darshan, B. Basavaraj, B. Daruka Prasad, S.C. Sharma, M.K. Sateesh, J.P. Shabaaz Begum, Arabian J. Chem. doi.org/10.1016/j.arabjc.2017.03.006.
38. X. Liu, K. Zhou, L. Wang, B. Wang, Y. Li, J. Am. Chem. Soc. 131(2009) 3140–3141.
39. Bin Xu, Qitao Zhang, Saisai Yuan, Ming Zhang, Teruhisa Ohno, Appl. Cataly. B: Envir. 183 (2016) 361–370.
40. J. Tauc, in: F. Abeles (Ed.), Optical Properties of Solids, North-Holland, Amsterdam, (1970) 277.
41. B. Choudhury, A. Choudhury, Curr. Appl Phys. 13 (2013) 217-223.
42. G.P. Ojha, B. Pant, S.J. Park, M. Park, H.Y. Kim, J. Colloid Interface Sci. 494 (2017) 338-344.
43. Ramachandra Naik, S.C. Prashantha, H. Nagabhushana, S.C. Sharma, H.P. Nagaswarupa, K.M. Girish, J. Alloys Compd. 682 (2016) 815-824.
44. H.B. Premkumar, D.V. Sunitha, H. Nagabhushana, S.C. Sharma, B.M. Nagabhushana, J.L. Rao, Kinshuk Gupta, R.P.S. Chakradhar, Spectrochim. Acta Part A: Mole. Biomole. Spect. 96 (2012) 154–162.
45. M. Venkataravanappa, H. Nagabhushana, G.P. Darshan, G.P., B. Daruka Prasad, G.R. Vijayakumar, H.B. Premkumar, Udayabhanu, Ultrason. Sonochem. 33 (2016) 226–239.
46. B.S. Ravikumar, H. Nagabhushana, S.C. Sharma, Y.S. Vidya, K.S. Anantharaju, Spectrochim. Acta, Part A, 136 (2015) 1027-1037.
47. M.L. Dos Santos, R.C. Lima, C.S. Riccardi, R.L. Tranquilin, P.R. Bueno, J.A. Varela, E. Longo, Mater. Lett. 62 (2008) 4509-4511.
48. Vijay singh, R.P.S. Chakradhar, J.L. Rao, Ho-Young Kwak, Solid State Sci. 11 (2009) 870-874.
49. A. Sandhyarani, M.K. Kokila, G.P. Darshan, R.B. Basavaraj, B. Daruka Prasad, S.C. Sharma, T.K.S. Lakshmi, H. Nagabhushana, Chem. Eng. J. *Accepted Manuscript.*
50. D. Dvoranova, V. Brezova, M. Mazur, M.A. Malati, Appl. Catal. B, 37 (2002) 91-105.

ACCEPTED MANUSCRIPT

51. J.C. De Mello, H.F. Wittmann, R.H. Friend, Adv. Mater. 9 (1997) 230–232.
52. L.O. Palsson, A.P. Monkman, Adv. Mater. 14 (2002) 757–758.
53. P.B. Devaraja, D.N. Avadhani, H. Nagabhushana, S.C. Prashantha, S.C. Sharma, B.M. Nagabhushana, H.P. Nagaswarupa, B. Daruka Prasad, Mater. Charact. 97 (2014) 27-36.
54. J. Malleshappa, H. Nagabhushana, S.C. Prashantha, S.C. Sharma, N. Dhananjaya, C. Shivakumara, B.M. Nagabhushana, J. Alloys Compd. 612 (2014) 425-434.
55. H.B. Premkumar, B.S. Ravikumar, D.V. Sunitha, H. Nagabhushana, S.C. Sharma, M.B. Savitha, S. Mohandas Bhat, B.M. Nagabhushana, R.P.S. Chakradhar, Spectrochim. Acta, Part A 115 (2013) 234-243.

ACCEPTED MANUSCRIPT

Figure Captions:

Fig.1. (a) PXRD patterns, (b) W-H plots, (c) Rietveld refinement and (d) Packing diagram of CeO_2: Cr^{3+} (9 mol %) NP.

Fig.2. (a) DR spectra, (b) Energy band gap, (c) Raman studies and (d) FTIR spectra of CeO_2:Cr^{3+} (1-11 mol %) NPs.

Fig.3. SEM micrographs of CeO_2: Cr^{3+} (9 mol %) NP synthesized with various sonication time (1, 2, 3, 4, 5 and 6 h) while concentration of *C. A.* seed extract and pH were fixed at 30% W/V and 13 respectively.

Fig.4. SEM micrographs of CeO_2: Cr^{3+} (9 mol %) NP synthesized with different concentration of *C. A.* seed extract (5, 10, 15, 20, 25 and 30 % W/V) with 6 h sonication time and pH value = 13.

Fig.5. Egg box model to explain the trapping mechanism of CeO_2:Cr^{3+} ions by the *Calycosin* isoflavone compound.

Fig.6. SEM micrographs of CeO_2: Cr^{3+} (9 mol %) NP synthesized with different pH values (3, 5, 7, 9, 11 and 13) while concentration of *C. A.* seed extract and sonication time were fixed at 30% W/V and 6 h respectively.

Fig.7. Schematic diagram of growth mechanism of 3D CeO_2: Cr^{3+} (9 mol %) NP synthesized by using ultrasound assisted sonochemical route with different sonication time, *C. A.* seed extract and pH values.

Fig.8.(a) TEM image, (b) SAED pattern and (c) HRTEM image of CeO_2: Cr^{3+} (9 mol %) NP.

Fig.9. (a) PL excitation spectrum and (b) Emission spectra of CeO_2:Cr^{3+} (1-11 mol %) NPs excited at 471 nm wavelength.

Fig.10. (a) Tanabe-Sugano energy level diagram of Cr^{3+} ions in CeO_2 (b) variation of PL intensity at 732 and 689 nm peak with different Cr^{3+} concentration (c) CIE and (d) CCT diagram of CeO_2:Cr^{3+} (1-11 mol %) NPs. [Inset: CIE and CCT values of CeO_2:Cr^{3+} NPs]

Fig.11. LFPs under UV 254 nm visualized by CeO_2:Cr^{3+} (9 mol %) NP synthesized by ultrasound method on: (a) glass under visible light, (b) glass, (c) plastic sheet, (d) stainless steel scale, (e) aluminum foil, and (f) Indian coins under UV 254 nm light.

Fig.12. LFPs visualized by CeO_2:Cr^{3+} (9 mol %) NP on various porous surfaces under UV 254 nm light.

Table Captions:

Table.1 Major isolated bio-active compounds in *C.A.* seed extract.

Table 2: Estimated average crystallite size, strain, energy band gap and oxygen vacancies of CeO_2:Cr^{3+} (1- 11 mol %) NPs.

Table 3: Rietveld refinement parameters of the CeO_2:Cr^{3+} (1- 11 mol %) NPs.

Table 4: Photometric characterizations of CeO_2:Cr^{3+} (1-11 mol %) NPs.

ACCEPTED MANUSCRIPT

Table.1 Major isolated bio-active compounds in *C.A.* seed extract.

Sl. No.	Chemical name	Structure
1.	*Calycosin (7,30-dihydroxy-40-methoxyisoflavone)*	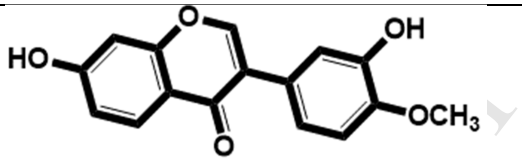
2.	*Formononetin (7-hydroxy-40-methoxyisoflavone)*	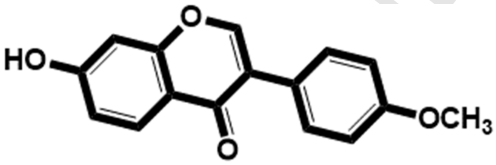
3.	*Genistein (5,7,40-trihydroxyisoflavone)*	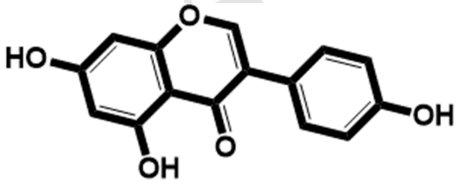
4.	*Trifolirhizin (maackiain-3-O-b-D-glucopyranoside)*	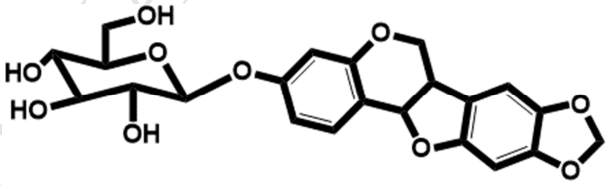
5.	*Ononin (7-O-b-D-glucosyl-7-hydroxy-40-methoxyisoflavone)*	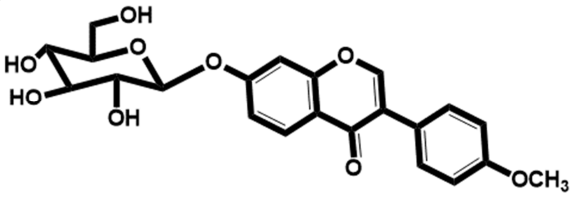
6.	*Sissotrin (7-O-b-D-glucosyl-5,7-dihydroxy-40-methoxyisoflavone)*	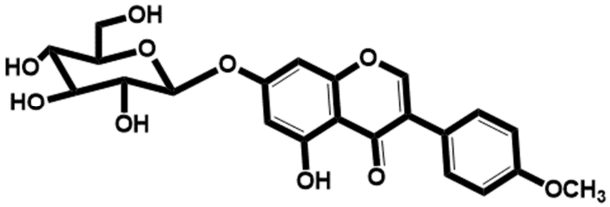

Table 2: Estimated average crystallite size, strain, energy band gap and oxygen vacancies of $CeO_2:Cr^{3+}$ (1- 11 mol %) NPs.

$CeO_2:Cr^{3+}$ (mol %)	**Crystallite size(nm)**		**Strain (x 10^{-4})**	**E_g (eV)**	**Area oxygen vacancies/area F_{2g} (%)**
	[Scherrer's approach]	**[W-H plots]**			
1	10	9	1.5	3.5	7.2
3	10	9	1.6	3.53	11
5	9	8	1.2	3.51	11.5
7	8	8	1.3	3.44	11.9
9	7	7	1.6	3.41	12.1
11	6	5	1.8	3.61	10.2

ACCEPTED MANUSCRIPT

ACCEPTED MANUSCRIPT

Table 3: Rietveld refinement parameters of the CeO_2:Cr^{3+} (1- 11 mol %) NPs.

Cr^{3+}conc.	Pure	1 mol %	3 mol %	5 mol %	7 mol %	9 mol %	11 mol %
Crystal system	Cubic	Cubic	Cubic	Cubic	Cubic	Cubic	Cubic
Space group	F m -3 m (225)	F m -3 m (225)	F m -3 m (225)	F m -3 m (225)	F m -3 m (225)	F m -3 m (225)	F m -3 m (225)
				Lattice parameters (Å)			
a=b=c	5.431	5.447	5.443	5.449	5.445	5.448	5.437
Unit cell volume ($Å^3$)	160.226	161.62	161.26	161.82	161.44	161.70	160.74
				Atomic co ordinates			
				Ce			
x	0.0000	0.0000	0.0000	0.0000	0.0000	0.0000	0.0000
y	0.0000	0.0000	0.0000	0.0000	0.0000	0.0000	0.0000
z	0.0000	0.0000	0.0000	0.0000	0.0000	0.0000	0.0000
Occupancy	1.3118	1.0000	1.0000	1.0021	1.0021	1.0021	1.0021
				Cr			
x	----------	0.0000	0.0000	0.0000	0.0000	0.0000	0.0000
y	----------	0.0000	0.0000	0.0000	0.0000	0.0000	0.0000
z	----------	0.0000	0.0000	0.0000	0.0000	0.0000	0.0000
Occupancy	----------	1.0000	1.0000	1.0021	1.0021	1.0021	1.0021
				O			
x	0.25000	0.2500	0.2500	0.2500	0.2500	0.2500	0.2500
y	0.25000	0.2500	0.2500	0.2500	0.2500	0.2500	0.2500
z	0.25000	0.2500	0.2500	0.2500	0.2500	0.2500	0.2500
Occupancy	2.27916	2.8045	2.6610	2.6244	2.6616	2.6880	2.6865
R_P	2.91	1.79	1.12	1.00	1.08	1.30	1.05
R_{WP}	3.97	3.22	2.46	1.23	1.36	1.59	1.35
R_{Exp}	9.17	9.22	5.89	4.10	5.79	5.92	5.89
$\chi 2$	0.187	0. 575	0.618	0.124	0.548	0.781	0.524
R_{Bragg}	1.83	1.418	1.561	1.227	1.283	1.263	1.141
R_F	1.54	1.470	1.601	1.204	1.290	1.237	1.117
X-ray density (g/cc^3)	6.961	6.870	6.833	6.803	6.826	6.827	6.856

Table 4: Photometric characterizations of CeO_2:Cr^{3+} (1-11 mol %) NPs.

Cr^{3+} Conc. (mol %)	**CIE**		**CCT (K)**	**CP (%)**
	X	**Y**		
1	0.7178	0.2820	7781	80
3	0.7093	0.2905	7047	79
5	0.6922	0.3075	5342	81
7	0.7105	0.2893	7152	82
9	0.7120	0.2878	7292	80
11	0.7051	0.2947	6580	81

ACCEPTED MANUSCRIPT

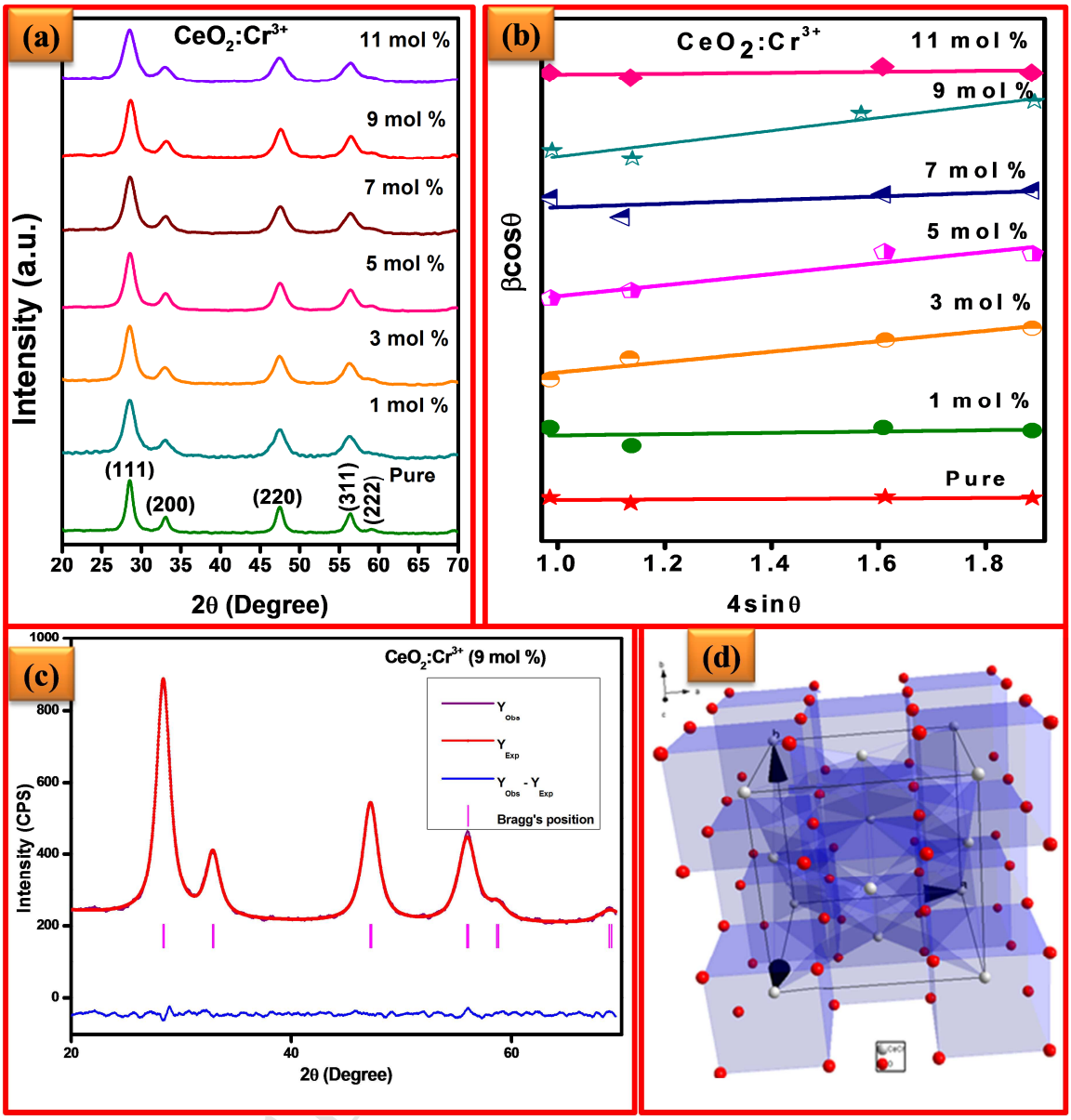

Fig.1. (a) PXRD patterns, (b) W-H plots, (c) Rietveld refinement and (d) Packing diagram of CeO_2: Cr^{3+} (9 mol %) NP.

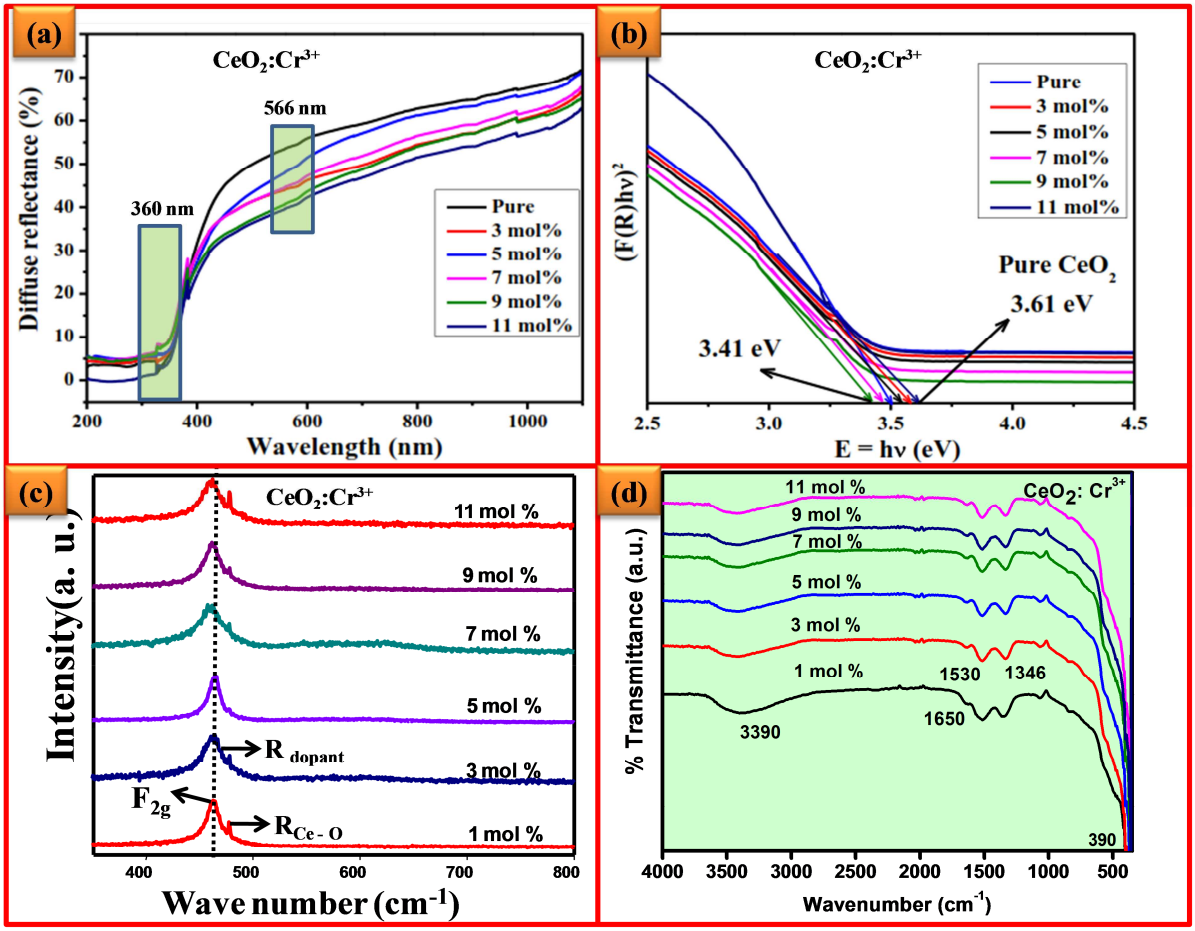

Fig.2. (a) DR spectra, (b) Energy band gap, (c) Raman studies and (d) FTIR spectra of CeO_2:Cr^{3+} (1-11 mol %) NPs.

ACCEPTED MANUSCRIPT

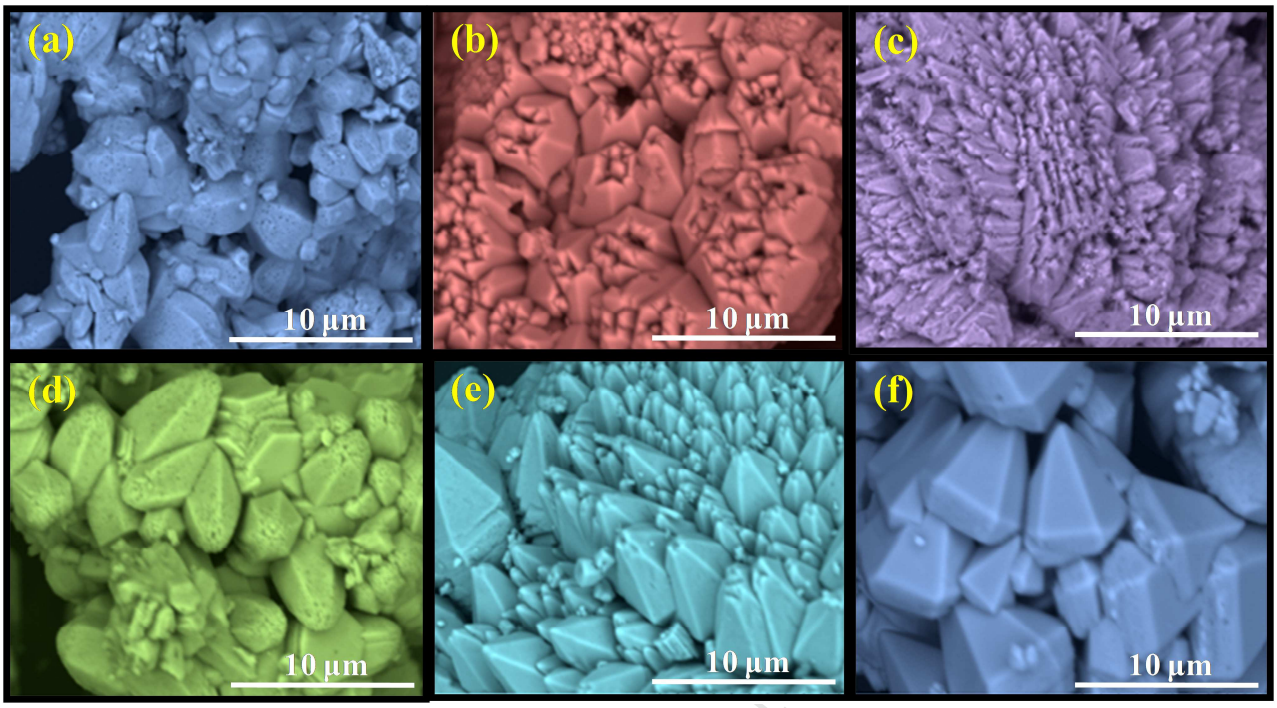

Fig.3. SEM micrographs of CeO_2: Cr^{3+} (9 mol %) NP synthesized with various sonication time (1, 2, 3, 4, 5 and 6 h) while concentration of *C. A.* seed extract and pH were fixed at 30% W/V and 13 respectively.

ACCEPTED MANUSCRIPT

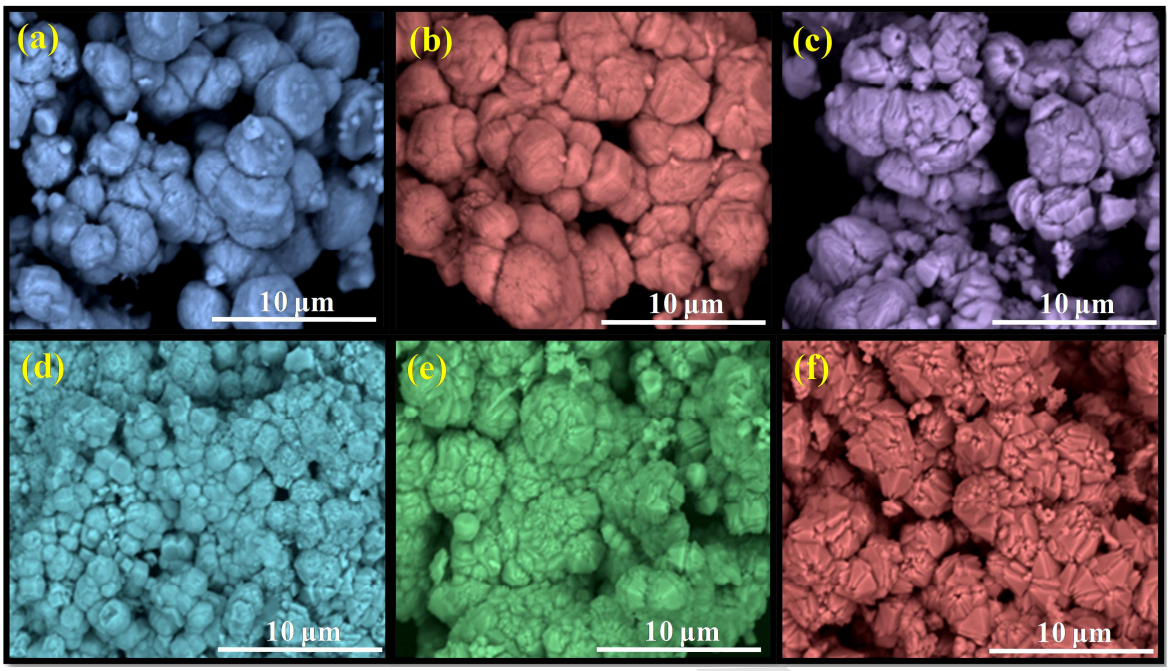

Fig.4. SEM micrographs of CeO_2: Cr^{3+} (9 mol %) NP synthesized with different concentration of *C. A.* seed extract (5, 10, 15, 20, 25 and 30 % W/V) with 6 h sonication time and pH value = 13.

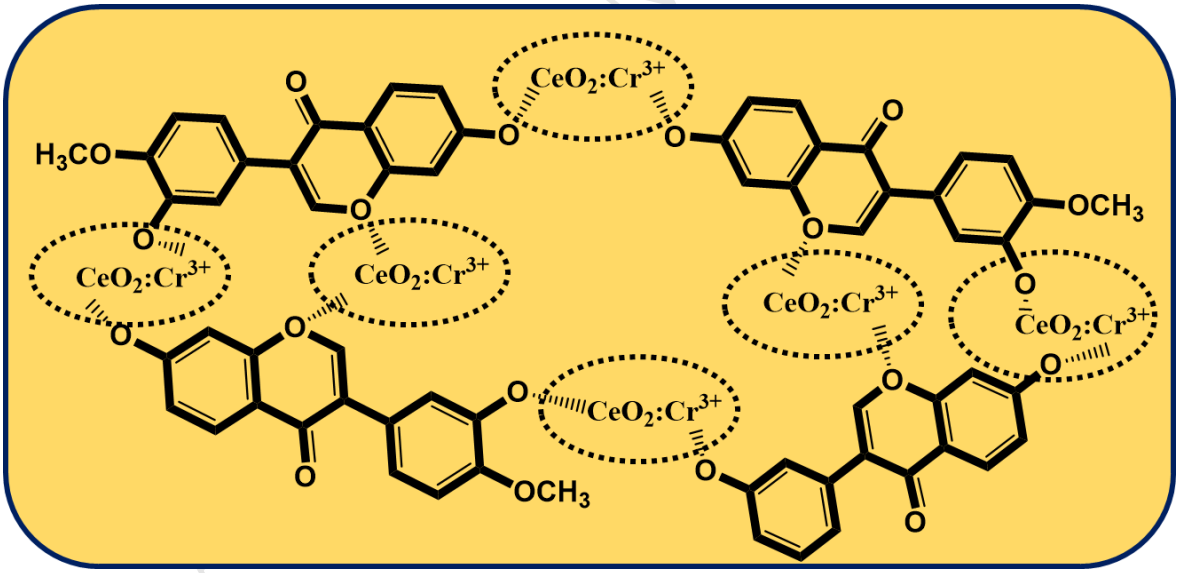

Fig.5. Egg box model to explain the trapping mechanism of CeO_2:Cr^{3+} ions by the *Calycosin* isoflavone.

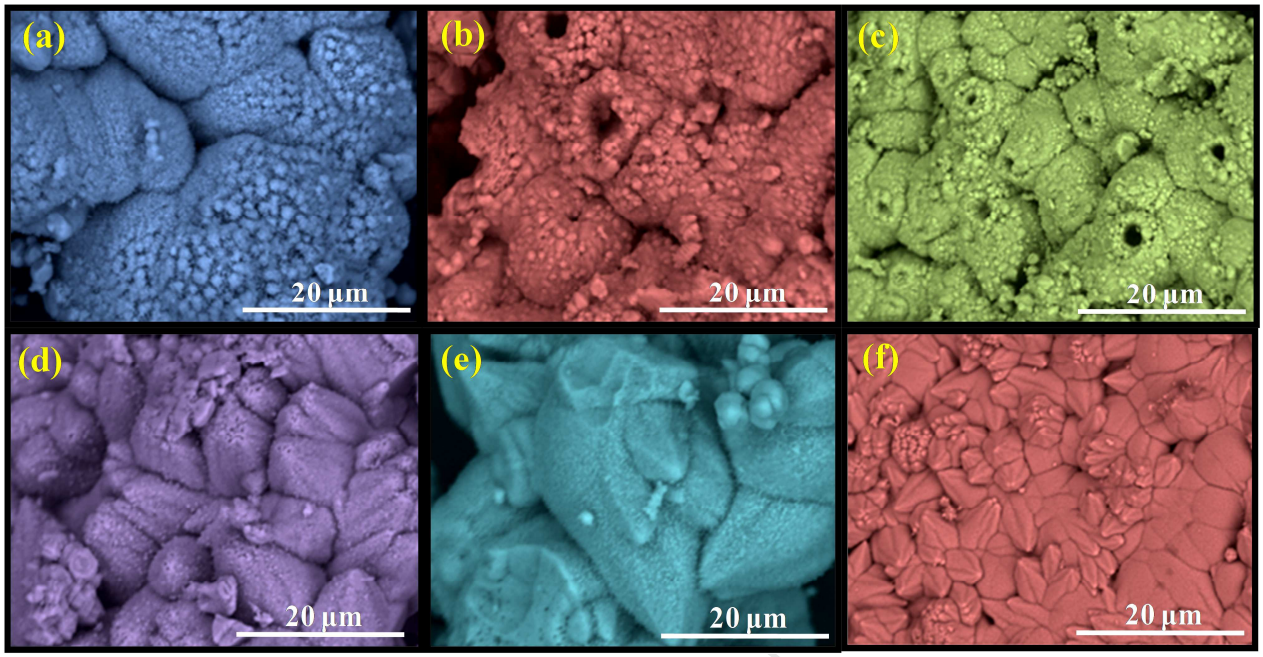

Fig.6. SEM micrographs of CeO_2: Cr^{3+} (9 mol %) NP synthesized with different pH values (3, 5, 7, 9, 11 and 13) while concentration of *C.A.* seed extract and sonication time were fixed at 30% W/V and 6 h respectively.

ACCEPTED MANUSCRIPT

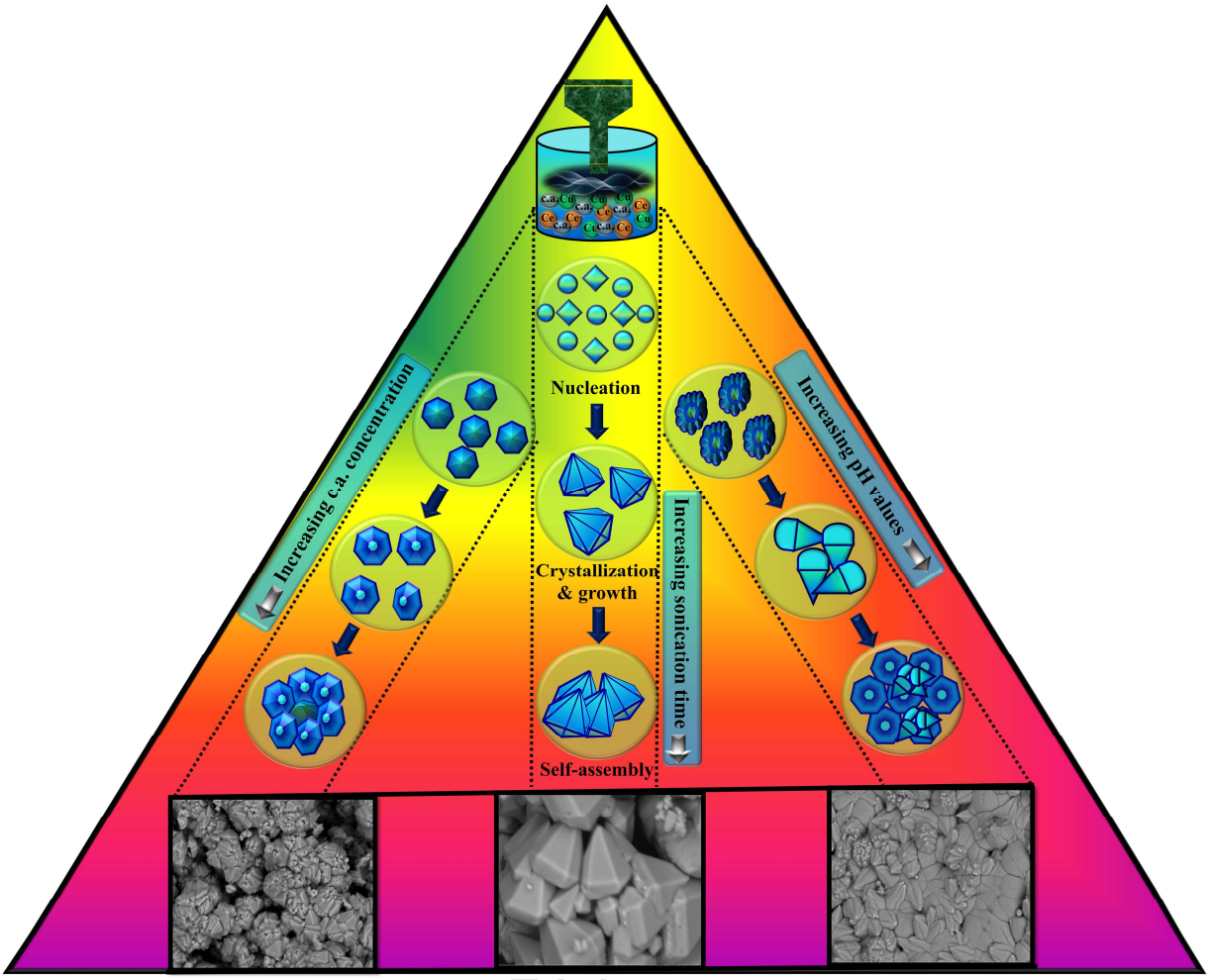

Fig.7. Schematic diagram of growth mechanism of 3D CeO_2: Cr^{3+} (9 mol %) NP synthesized by using ultrasound assisted sonochemical route with different sonication time, *C. A.* seed extract and pH values.

ACCEPTED

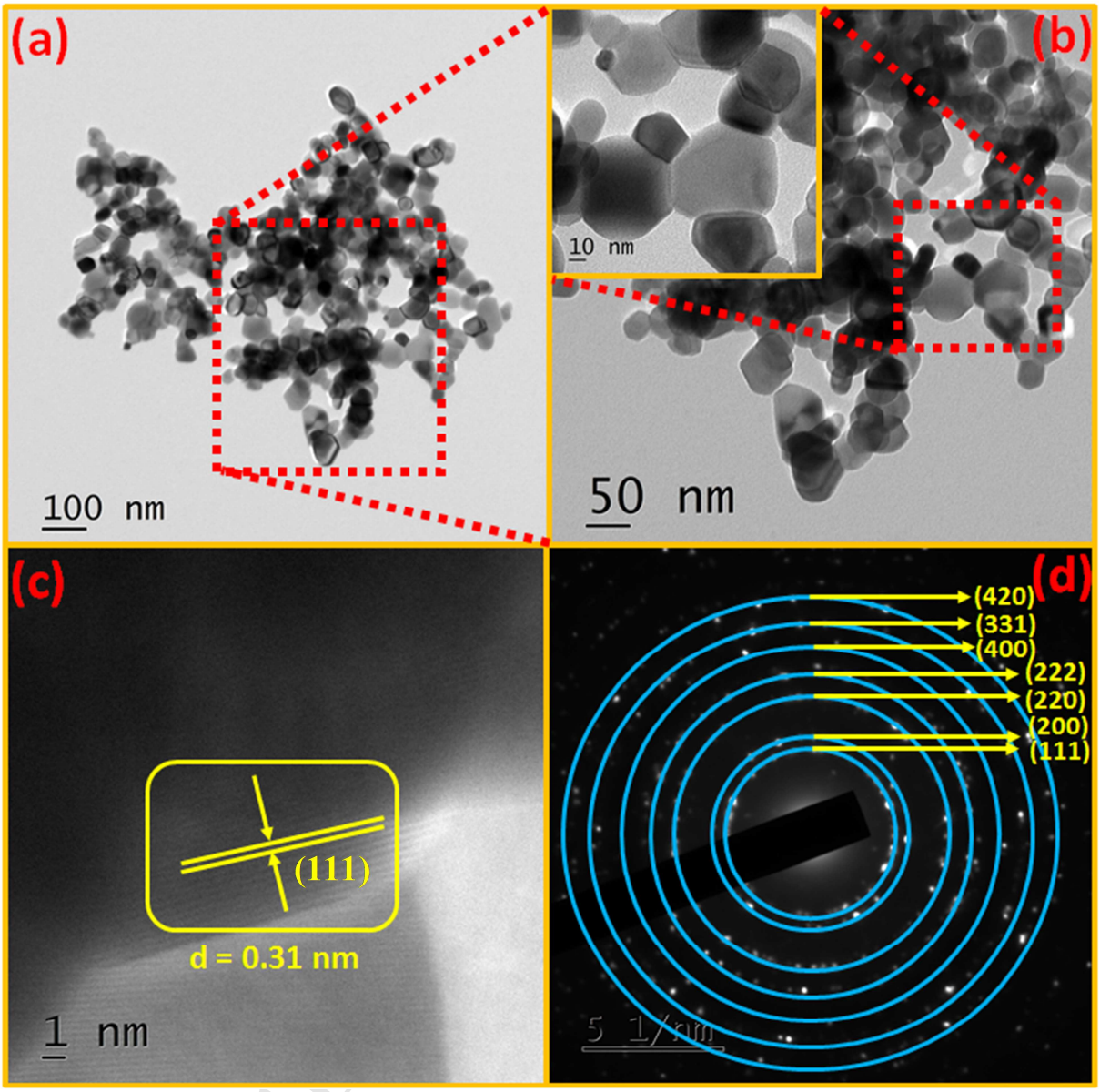

Fig.8.(a, b) TEM image,(c) HRTEM and (d) SAED pattern image of CeO_2: Cr^{3+} (9 mol %) NP.

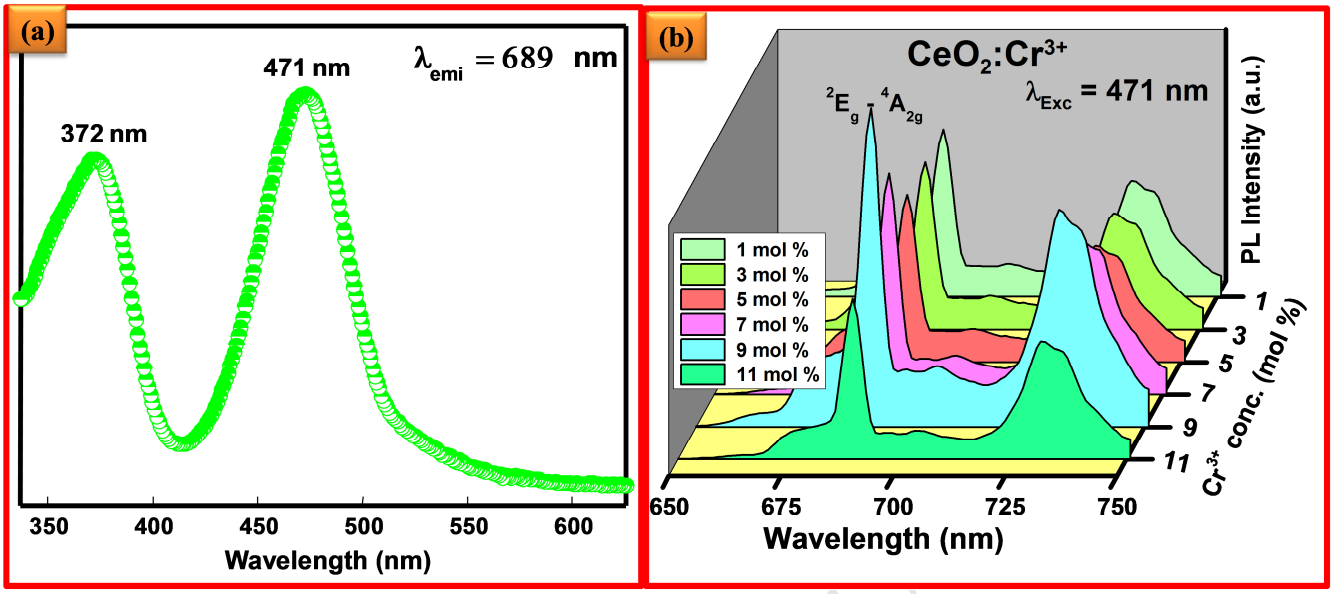

Fig.9. (a) PL excitation spectrum and (b) Emission spectra of $CeO_2:Cr^{3+}$ (1-11 mol %) NPs excited at 471 nm wavelength.

ACCEPTED MANUSCRIPT

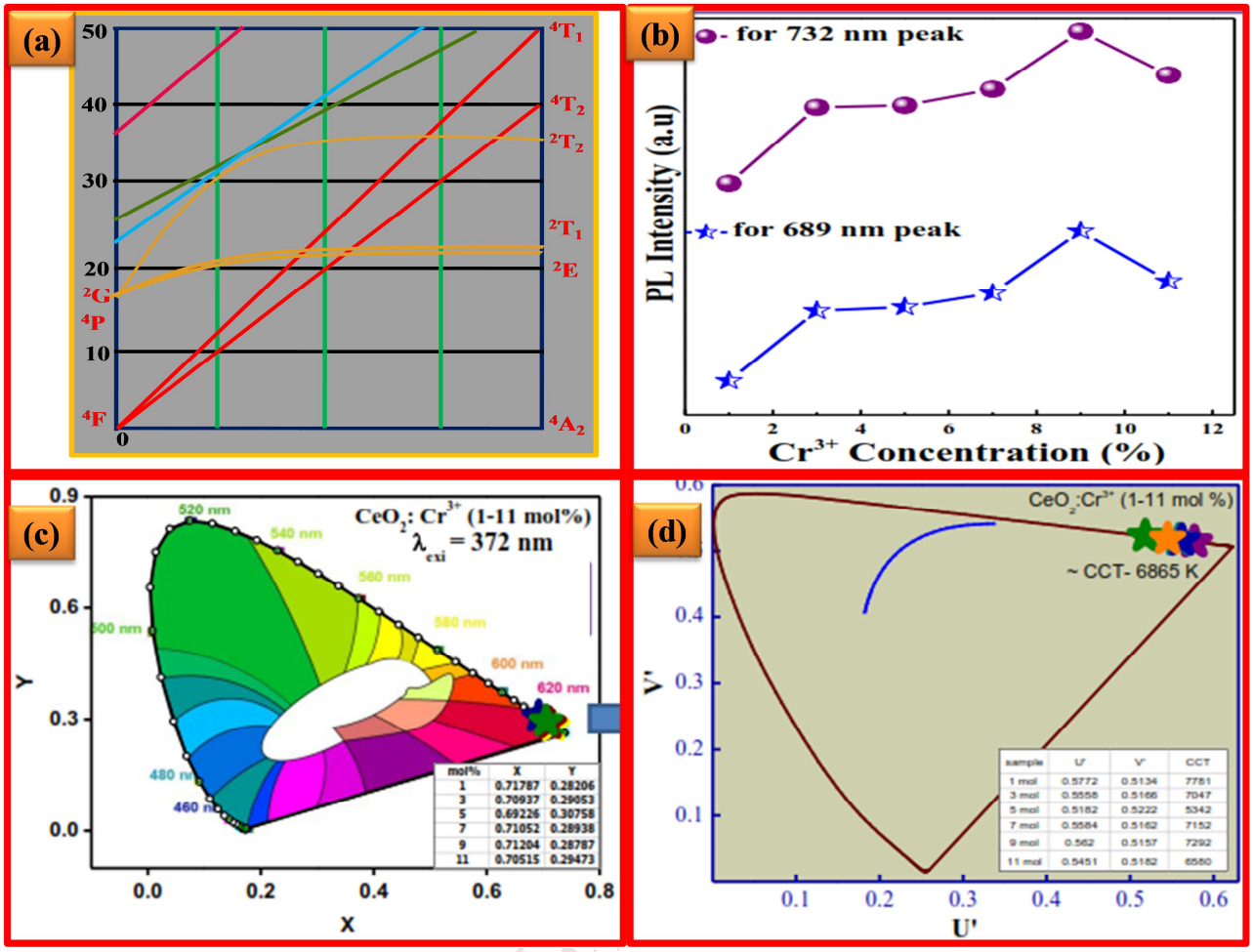

Fig.10. (a) Tanabe-Sugano energy level diagram of Cr^{3+} ions in CeO_2 (b) variation of PL intensity at 732 and 689 nm peak with different Cr^{3+} concentration (c) CIE and (d) CCT diagram of CeO_2:Cr^{3+} (1-11 mol %) NPs. [Inset: CIE and CCT values of CeO_2:Cr^{3+} NPs]

ACCEPTED

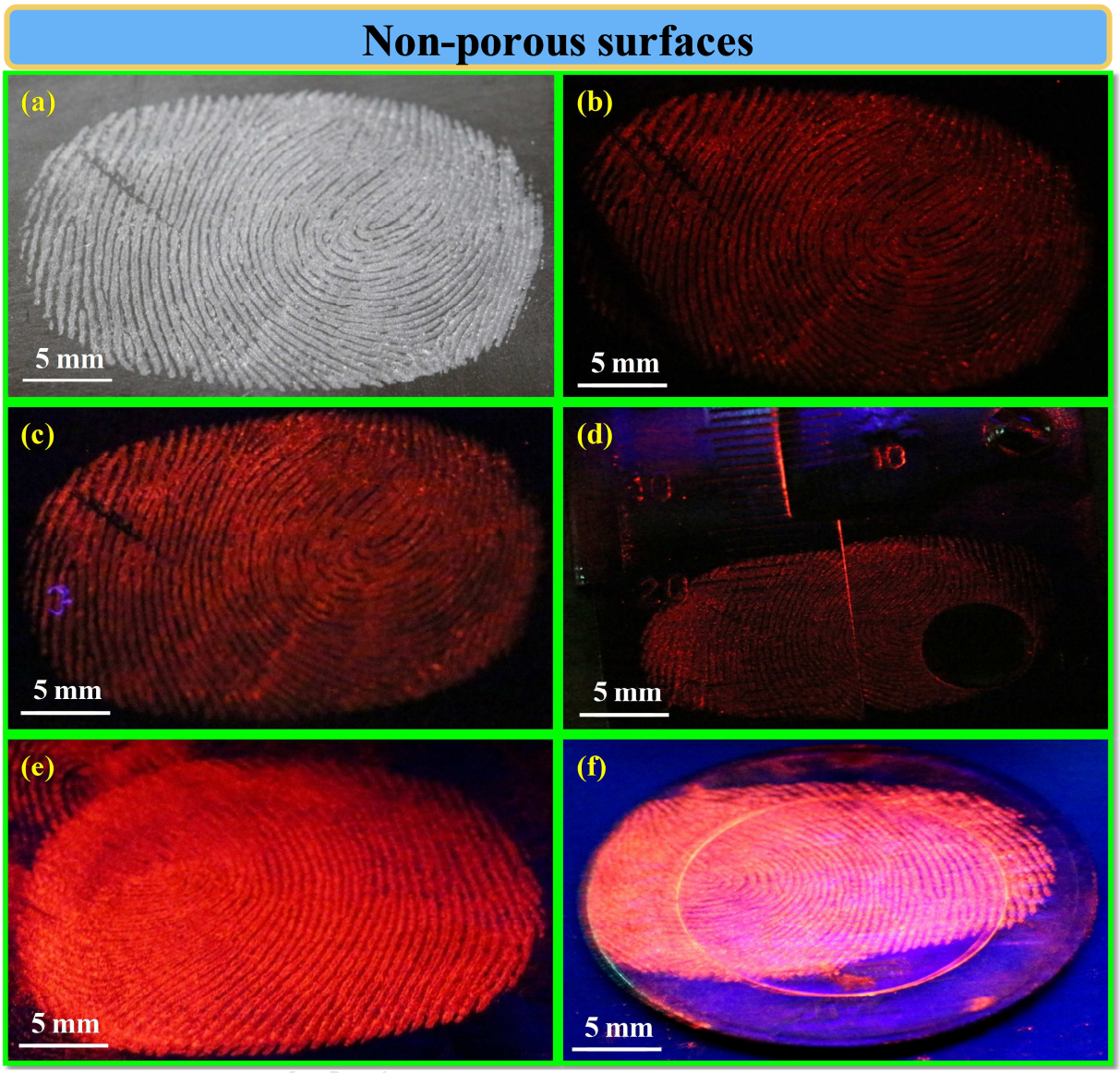

Fig.11. LFPs under UV 254 nm visualized by $CeO_2:Cr^{3+}$ (9 mol %) NP synthesized by ultrasound method on: (a) glass under visible light, (b) glass, (c) plastic sheet, (d) stainless steel scale, (e) aluminum foil, and (f) Indian coins under UV 254 nm light.

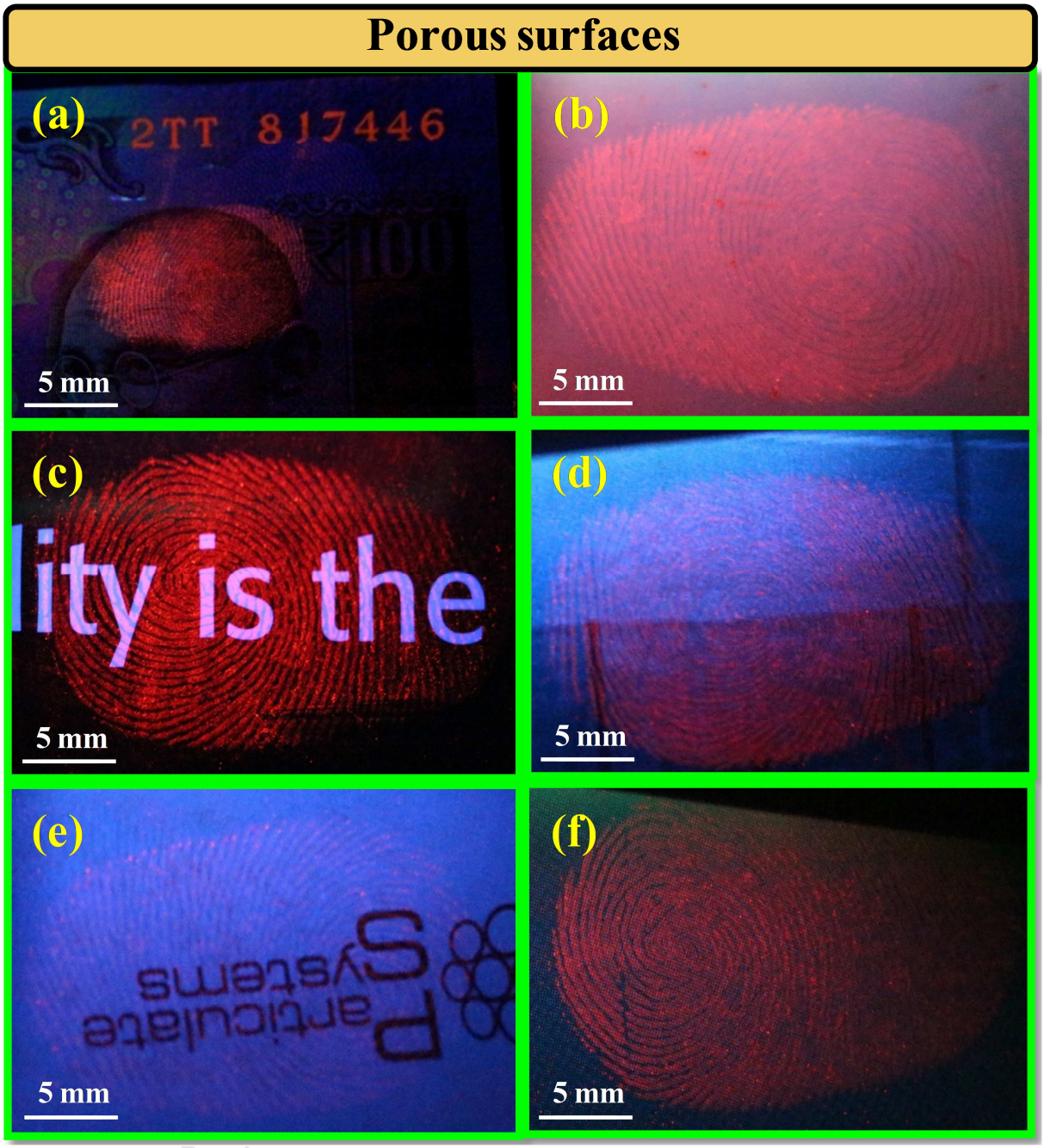

Fig.12. LFPs visualized by $CeO_2:Cr^{3+}$ (9 mol %) NP on various porous surfaces under UV 254 nm light.

ACCEPTED MANUSCRIPT

Research Highlights

1. CeO_2:Cr^{3+} (1-11 mol %) nanophosphors were prepared by facile bio-template assisted ultrasonication route.

2. The obtained samples displayed 3D superstructures of various morphological shapes.

3. The optimized product was used for forensic and LED's applications.

ACCEPTED MANUSCRIPT